An apparatus for temperature-dependent soft X-ray resonant magnetic scattering

Nicolas Jaouen,[a]* Jean-Marc Tonnerre,[a] Grigor Kapoujian,[a] Pierre Taunier,[a] Jean-Paul Roux,[a] Denis Raoux[a] and Fausto Sirotti[b]

[a]Laboratoire de Cristallographie, CNRS, BP 16, 25 Avenue des Martyrs, 38042 Grenoble, France, and [b]Laboratoire pour l'Utilisation du Rayonnement Electromagnétique, Batiment 209D, Université Paris-Sud, 91405 Orsay, France. E-mail: jaouen@esrf.fr

Interest in the use of soft X-ray resonant magnetic scattering techniques to probe the distribution of magnetic moments in thin films has exploded during the last few years. In this paper a novel diffractometer devoted to temperature-dependent soft X-ray resonant scattering is described. The principal features of the diffractometer are presented and illustrated through experiments performed at LURE during the commissioning phase.

Keywords: X-ray magnetic scattering.

1. Introduction

Although the first demonstration of the existence of magnetic X-ray scattering was performed 20 years ago, it is only recently that the investigation of subtle magnetic effects and properties *via* the resonant scattering of polarized soft X-rays has attracted wide interest, *e.g.* the observation of large magnetic dichroic asymmetry ratios in reflection experiments at the Fe and Co $L_{2,3}$ edges (Kao *et al.*, 1990, 1994). For example, it permits the extraction of magnetic depth-resolved information in artificial multilayers (Jaouen *et al.*, 2001). Also, purely magnetic diffraction peaks in superlattices owing to the antiferromagnetic order between ferromagnetic layers have been observed (Sève *et al.*, 1995; Tonnerre *et al.*, 1995) and extensively studied more recently (Hase *et al.*, 2000; Spezzani *et al.*, 2002), and another recent experiment on striped magnetic domain structures that exhibit perpendicular magnetic anisotropy has been reported (Dürr *et al.*, 1999). These measurements demonstrate that diffraction experiments carried out in the soft X-ray range match perfectly the nanometer length scale of artificial magnetic structures. Stimulated by the technological impact of the discovery of effects such as perpendicular magnetic anisotropy and giant magnetoresistance effects, several groups have adapted old chambers (Roper *et al.*, 2001) or built *at nuovo* dedicated instruments for X-ray resonant magnetic scattering in the soft X-ray range (Johnson *et al.*, 1992) with the focus on surface science (Sacchi *et al.*, 2003) or transportability (Grabis *et al.*, 2003).

At the Laboratoire de Cristallographie, we began our activity in this field in 1993 by performing the first experiment on an in-vacuum diffractometer, initially designed for test multilayers with soft X-rays (Tonnerre *et al.*, 1993). Based on our experience through different collaborations, we have developed a dedicated large-volume diffractometer designed to work under high vacuum, at low temperature and with a reasonably high magnetic field.

The first part of this paper will be dedicated to the description of this new apparatus, and its performance will be illustrated in the second part through two examples of experiments performed during the commissioning phase. Future instrumentation developments, taking advantage of the huge volume of the vacuum chamber, will be mentioned in the conclusion.

2. Instrument design

2.1. UHV chamber

The strong absorption of soft X-rays by air made it necessary to develop an in-vacuum system. With the aim of building a chamber which allowed further evolution, a large-volume chamber has been designed, shown three-dimensionally in Fig. 1. It is composed of two main parts: a cylindrical vessel of diameter 90 cm and height 40 cm, and a large flange which carries several components (differentially pumped rotary seal, sample manipulator, cryostat and electromagnet). This flange is labelled the θ assembly (Fig. 1 top). At the bottom of the vessel, a crown (1) is attached to a differentially pumped rotary seal (2) and carries the detector (3). This group of components is called the 2θ assembly (Fig. 1 bottom). The whole chamber is attached to a support by two rotatory platforms (Fig. 2) allowing rotation of the chamber axis along the beam path. Therefore it is possible to change the diffraction geometry from vertical to horizontal. It should be stated, however, that at the moment this change of configuration cannot be performed when the chamber is connected to the beamline. This capability was initially designed in order to take full advantage of the synchrotron radiation beam characteristics provided by different beamlines, such as the polarization state, shape of the focus spot and divergence. However, it is of

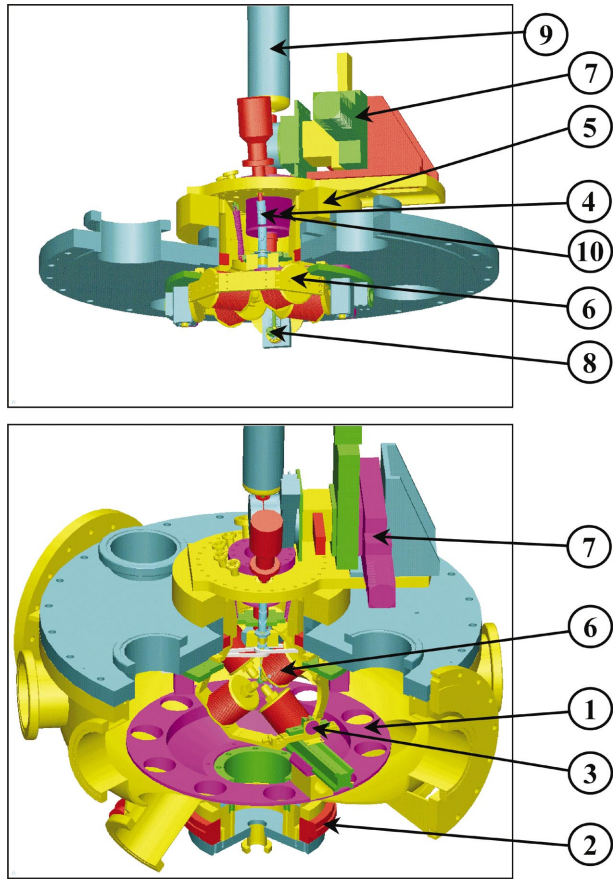

Figure 1
Three-dimensional view of the diffractometer. The top and bottom panels display the θ and the 2θ assemblies, respectively. The numbering is used in the text for better understanding.

 DOI: 10.1107/S0909049504013767

less interest today since several soft X-ray beamlines are equipped with undulators that can produce right- and left-circular polarized light as well as both horizontal and vertical linearly polarized light [see for example ID8 at ESRF (Goulon *et al.*, 1995) and the SIM beamline at the Swiss Light Source (Quitmann *et al.*, 2001)].

All of the motors allowing sample actuation and detector rotation, as well as sample translations, are kept outside of the vacuum chamber, with the motions being transmitted through a bellow (4) and a second differential-pumped rotary seal (5). The goal was to reach the best possible ultimate vacuum condition in order to reduce the formation of a contamination layer at the surface of the sample which could affect the intensity of the reflected X-ray beam when the sample is cooled. For this purpose, 316L stainless steel, or that of a similar quality with a low carbon content, has been used and the chamber was fired at 1323 K for 3 h at $<10^{-5}$ mbar. Additionally, the internal surface has been treated by shotblasting.

Pre-pumping of the chamber is achieved by a scroll-type dry pump. Vacuum pumping is performed by a $520\,l\,s^{-1}$ turbo-drag pump connected to a CF160 UHV flange and backed by a $70\,l\,s^{-1}$ turbo pump, itself backed by a dry rough pump. Final low pressure may be reached by using a Ti sublimation pump associated with a liquid-nitrogen-cooled cryo-panel installed on a second CF160 UHV flange. A final CF160 port is left free for eventually attaching an ion pump. Furthermore, an independent dry pumping group, based on a $65\,l\,s^{-1}$ turbo-molecular pump and an oil-free membrane pump, is used for the two differentially pumped rotary feedthroughs. A base pressure of 3×10^{-9} mbar has been achieved with a continuous current of 8 A in the electromagnet. A magnetic drive and its carrying fork have been developed in order to transfer the sample into the chamber.

2.2. Goniometer

The two-circle goniometer consists of two motorized CF250 two-stage differentially pumped rotary feedthroughs. One is mounted on the θ assembly carrying an electromagnet (6) and a sample manipulator (7); the other is mounted on the opposite side, under the vessel carrying the detector arm. Sample and detector rotation can be driven independently. The experimental set-up is schematically shown in Fig. 2. The large size of the rotation feedthroughs ensures an accuracy of the axial angular motion which is largely sufficient in the soft X-ray range, allowing it to be free from additional precision rotary stages. A resolution and reproducibility smaller than 0.005° has been determined. This configuration has been preferred to that with both rotation stages on the same side in order to reduce the length of the shaft holding the sample holder, and hence reducing the cantilever and potential vibration at the sample position, especially when the diffraction axis is set horizontally. In order to relieve with ease the strain on the rotary feedthroughs when the rotation axis is set horizontally and to increase the precision of their concentricity, two additional ball bearings were installed inside the CF250 port of the vessel and inside that of the big flange. The rotating stages have been aligned and are concentric within 50 µm. To maintain the alignment of the two axes after the opening of the chamber, the top flange is positioned with the help of three pins at 120° one to the other. A helicoflex seal is used, and tightened using a 200 N m torque wrench to keep the rotation stages parallel within 50 µm.

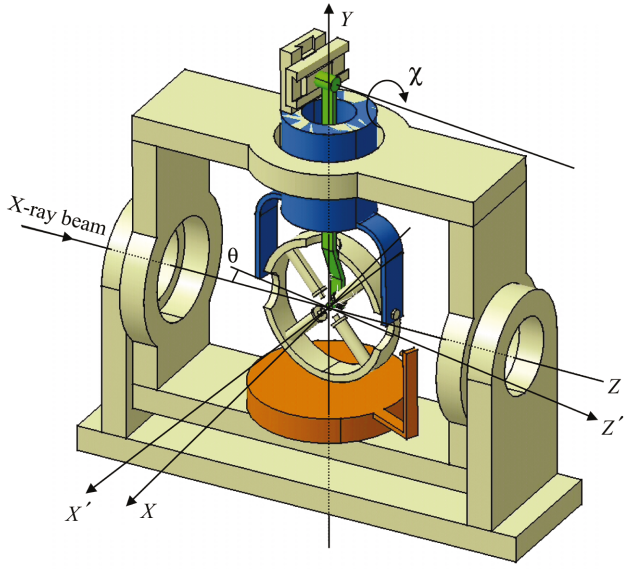

Figure 2
Sketch showing the goniometer movements and the sample environment.

2.3. Magnetic device

The electromagnet consists of two pairs of 20 mm-diameter cylindrical poles positioned in the YZ' plane at 45° from both the Y and Z' axes (Fig. 2). An octagonal ferromagnetic yoke supports the poles and guides the magnetic flux by providing a low-reluctance return path for the magnetic field. Both poles and yoke are made from pure iron. The poles pieces are 127.5 mm long and the tip-to-tip spacing is 25 mm. Each pole is excited by a 620 turn coil of 1.9 mm-diameter copper wire insulated with Kapton. The opposite poles are supplied in series so that the magnetic field is in the same direction in the poles. Each pair of poles is supplied independently, allowing the magnetic field to be orientated in any direction in the sample plane. Up to now, this setting has been used to reverse the magnetic field applied along the Z' or the Y axis (longitudinal and transverse configuration, respectively, if the scattering plane is XZ), as well as to change the amplitude of the applied magnetic field (hysteresis curves). We have mapped the magnetic field using a transverse Hall probe. The upper part of Fig. 3 shows the variation of the magnetic field magnitude along different axes for an excitation current, I, of 5 A in both pairs of coils. The magnetic field is homogeneous to within 1% in a volume of 1 mm × 1 mm × 1 mm and varies by 3.5% within 2 mm × 2 mm × 2 mm. The lower part of Fig. 3 shows the achieved magnetic field as a function of excitation current. The field increases linearly from 0 to 0.12 T when the excitation current is increased from 0 to 2 A. When an excitation current of 8 A is used, the applied magnetic field reaches an upper limit of 0.2 T. When the current is turned off, a remanent bias field of about 3×10^{-3} T remains at the centre. It is worth noting that these four coils can be moved away from the sample [*via* a rotational stage (10)] as shown in Fig. 2 (see also the top of Fig. 1 where the device is positioned horizontally and the bottom of Fig. 1 when it is positioned vertically). This capability has been developed for the investigation of systems that display a natural magnetic order, *e.g.* for systems showing perpendicular magnetic anisotropy (Dürr *et al.*, 1999). It also allows the sample holder to be locked onto the cold finger with the magnetic transfer device from the front.

2.4. Sample manipulator

Three orthogonal translations, along X', Y and Z', are provided for aligning the sample as well as for tilting the sample around Z', which is the combination of a χ rotation (whose axis is 418 mm from the sample) and the two translations along X' and Y (Fig. 2). Y defines the θ rotation axis, Z' lies in the sample surface and is rotated from

the Z axis (direction of the incident beam) by an angle θ, X' is normal to the sample surface and is also distinct from the X axis (perpendicular to the direction of incident beam) by an angle θ. All these four movements are independent of the magnetic device. Because of the unusual arrangement of the manipulator, the shaft carrying the sample holder is also connected to the CF250 plate by four drawback springs. This limits the sample holder displacement when the vacuum is set.

The amplitude of the sample translations is limited to ± 5 mm along the three directions from the central position in order to prevent either the sample holder (a hollow cylinder of diameter 16 mm) from touching the polar pieces of the magnetic device or the sample holder shaft from touching the upper part of the magnetic device framework (when this is positioned vertically).

The sample manipulator has four Microcontrole stepper-motor driver stages that control the sample position. In the case of the horizontal position of the vessel (Figs. 1 and 2), the sample height (Y axis) and position across the beam (X' axis) are realised within ± 0.5 µm resolution. The sample position along the Z' axis is used to set the sample in the cross-point of the four coils, also shown in Fig. 2. The resolution of this translation is 0.1 µm and was conceived in order to allow scanning of the sample in front of a microfocused beam. Finally, the χ rotation is performed with a resolution of 0.0004°. This circle allows us to set properly the surface of the sample with respect to the diffraction plane.

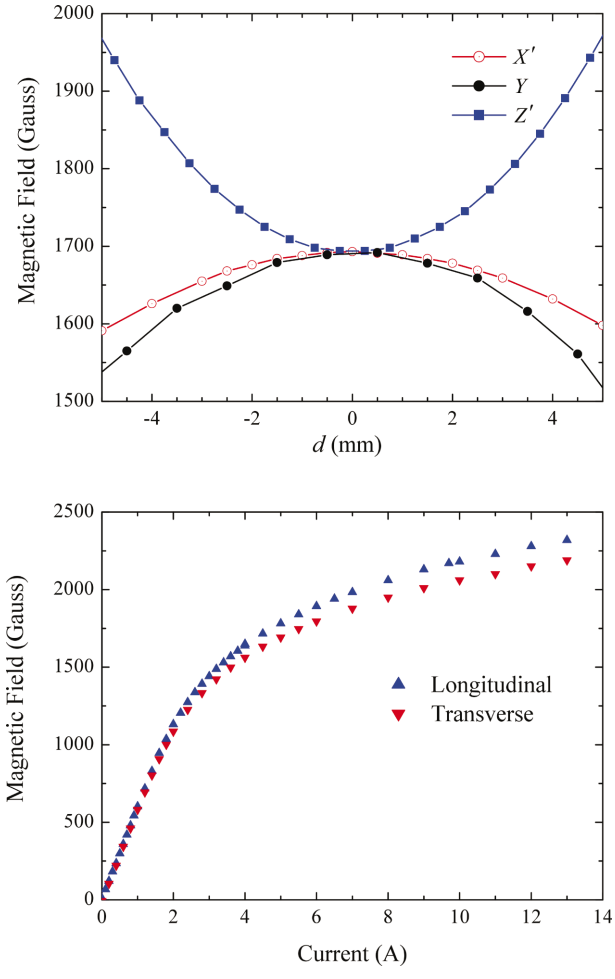

Figure 3
Magnetic calibration of the sample magnetization coils. (*a*) Amplitude change of the magnetic field at $I = 5$ A around the centre of the device along the X', Y and Z' directions. (*b*) Magnetic field amplitude at the centre *versus* applied current.

2.5. Cryostat

The sample holder is mounted on a copper cold finger (8) which is the final part of a continuous-flow helium cryostat system. The cold finger is set along the X' axis perpendicular to the plane of the four coils of the magnetic device. This orientation imposes us to design a special cryostat where the axis of the main body (9) is collinear with the rotation axis of the sample and with an end-part perpendicular to it. This elbow shape leaves some space around the sample holder and has been designed to bring the four iron poles of the electromagnet as close as possible to the sample holder. Despite heat loss from the coils, the cooling efficiency of this system was sufficient to reach 66 K at the sample during the test experiments. Recent results indicate that an ultimate temperature of 30 K can be stabilized.

2.6. Detection

The intensity of the diffracted beam is detected by a silicon photodiode (Canberra-Eurisys IP 300-PH-CER) with a sensitive area of diameter 21.5 mm. An electrometer is used for the readout of the signal. The detection limit, including the whole counting chain, is $\sim$0.5 pA. The diode is positioned behind a removable group of two slits that allow the setting of the angular divergence. An electrometer is used for the readout of the signal. Up to now, the incoming-beam intensity is monitored using the host beamline system. During the commissioning, this signal was measured from the drain current from a gold mesh and used to correct the effects of beam decay and variations in the incident flux.

2.7. Control

The diffractometer is completely controlled by a PIII 500 PC running SPEC software† in a Linux environment. For data acquisition, a GPIB (IEEE 488) interface is used to control the electrometers and the power supplies of the magnetic device. The six other motors are connected *via* serial interfaces. The menu-driven software provides the flexibility to perform multidimensional scans directly. Moreover, *via* macro files it allows complex measurement sequences to be built up quickly as the demands of the experiments dictate. For example, reversing the magnetization direction at each point of the measurement or scanning the reciprocal space along a particular path is currently possible.

3. First experimental results

The diffractometer described above was commissioned at LURE on the SB7 beamline (Sirotti *et al.*, 2000) at the SuperACO storage ring. This beamline uses a 'dragon-type' monochromator and is equipped with a double vertical-focusing mirror in order to allow for fast switching of light polarization.

Here, the performance of the instrument will be illustrated by a brief description of two selected experiments.

The first experiment concerns X-ray resonant magnetic scattering measurements carried out on a $Fe_{70}Mn_{30}$ alloy film of thickness 23 Å. The film is epitaxially grown on an Ir buffer layer and capped by a 30 Å Ir layer both to prevent the alloy from oxidation and to apply a similar strain at the two interfaces of the magnetic layer (Fischer, 1995). The trilayer system has been grown on an Al_2O_3 substrate.

† The SPEC software is a commercial package for diffractometer control that is available from Certified Scientific Software, PO 390640, Cambridge, MA 02139, USA (http://www.certif.com).

Fig. 4 shows an example of angular-dependent specular reflectivity measured at a fixed photon energy (707.1 eV) close to the Fe $L_{2,3}$ absorption edge. At each angular position the scattered intensity is recorded for both parallel (I^+) and antiparallel (I^-) orientations of the sample magnetization and the incident photon helicity. A saturating magnetic field has been applied parallel to the surface and in the diffraction plane. The asymmetry ratio, defined as $R = (I^+ - I^-)/(I^+ + I^-)$, is shown in the bottom panel of Fig. 4. The angular range limitation observed in this curve has to be related to the limited flux available at the SB7 bending-magnet beamline. We point out an abrupt increase of the asymmetry ratio at about 17°. This is due in part to the magnetic contrast observed in the dip in the reflectivity at 17°, and also due to the normalization by the charge reflectivity in R which is reduced at that specific angular position. The energy dependence of the scattered intensity at a given angle was also recorded and one example is displayed in Fig. 5. The value of the scattering angle θ was fixed at 5° and the detector at 10°. The incoming photon energy was scanned across the Fe 2p resonance. Again the external magnetic field was reversed at each point of the measurement.

These spectra are extracted from an investigation of the Ir/Fe_xMn_{1-x}/Ir trilayer (Bontempi *et al.*, 2004) where the motivation is to determine the changes in the magnetic properties of the alloy (magnetic moment amplitude of Fe and Mn atoms, their relative orientation and their amplitude distribution throughout the layer) when the concentration of Mn is varied from 10 to 30%. As Fe and Mn do not have the same elastic constant, this composition variation induces a change in the interfacial strain inside the film and consequently a change in the c/a parameter related to a change in the magnetic properties (Déchelette, Saint-Lager *et al.*, 1999).

The full lines in the bottom panel of Fig. 4 and in the right-hand panel in Fig. 5 are a simulation of the experiment. The calculation has been performed with the structural parameters derived from the refinement of the hard X-ray reflectivity measurements. The imaginary part of the resonant atomic scattering factor was derived from X-ray absorption spectroscopy (charge contribution) and from X-ray magnetic circular dichroism (magnetic contribution) for a thick iron film and for a Mn ultrathin film deposited on an Fe substrate (Déchelette, Tonnerre *et al.*, 1999). The real part of the charge and the magnetic atomic scattering factors are simply derived from the Kramers–Kronig transformation. In order to fit the data at the Fe $L_{2,3}$ edge, the Fe XMCD amplitude (which corresponds to a 3d magnetic moment of 2.1μ_B) has been reduced by an average weighting factor equal to 0.33, which yields a reduced magnetic moment of the Fe in the $Fe_{70}Mn_{30}$ thin alloy film of 0.7μ_B. Moreover, the adjustment of the angular-dependent asymmetry ratio (Fig. 4) above 17.5° required a larger reduction of the magnetic moment at the interface. Interestingly, the energy dependence of the asymmetry ratio display in Fig. 5 looks similar to the Faraday rotation spectra already published in the literature (Kortright & Kim, 2000). However, several differences can easily distinguish between these two experimental results. Here, we measured the intensity change in the reflectivity condition, and the asymmetry ratio is a cross-term mixing the real and imaginary part of the charge and magnetic contributions, hence modifying the spectral shape especially when dealing with successive interfaces. In these calculations, the precise knowledge of the structural parameters is extremely important in order to reproduce the angular-dependent reflectivity (Fig. 4) as well as the energy-dependent reflectivity (Fig. 5). This last point underlines the necessity of calculations including properly determined structural parameters (layers density, thicknesses and roughness) if one intends to extract quantitative information from X-ray resonant magnetic reflectivity data.

The second example concerns the study of the exchange coupling between a rare-earth and a transition metal layer through a metallic spacer by X-ray resonant magnetic reflectivity. In this case, our motivation was to investigate, below and above the Gd Curie temperature, the magnetic distribution at the interfaces of the magnetic layers and the magnetic profile throughout the spacer layer. Our first measurements were carried out from a [Gd(35 Å)/Cr(12 Å)/Co(45 Å)] trilayer. In order to illustrate the possibilities of measuring element-specific hysteresis loops, Fig. 6 shows the magnetization curves at 66 K recorded with the incident photon energy tuned close to the Co L_3 edge (778 eV) and to the Gd M_5 edge (1181 eV).

We simply recorded the scattered intensity as a function of the intensity and direction of the applied magnetic field. Moreover, by

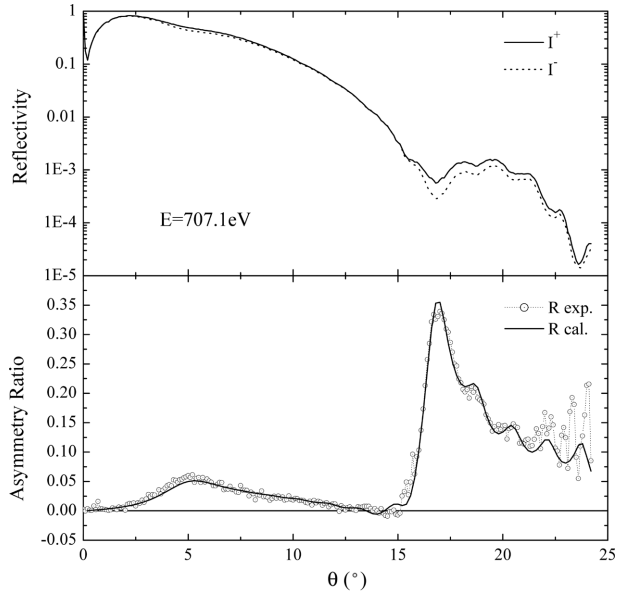

Figure 4
X-ray resonant magnetic scattering at the Fe L_3 edge from an Ir/$Fe_{70}Mn_{30}$/Ir/Al_2O_3 thin film. Top: scattered intensity as a function of the incident angle. Solid and dashed lines are for opposite directions between sample magnetization and photon helicity. Bottom: experimental and calculated asymmetry ratio (see text).

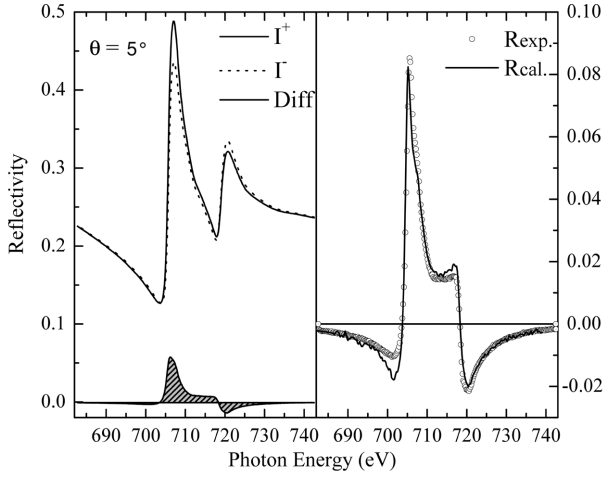

Figure 5
Energy-dependent reflectivity ($\theta = 5°$) at the Fe L edges for an Ir/$Fe_{70}Mn_{30}$/Ir/Al_2O_3 thin film. Solid and dashed lines in the left-hand panel are for opposite directions between sample magnetization and photon helicity. The right-hand panel shows the experimental and calculated asymmetry ratio (see text).

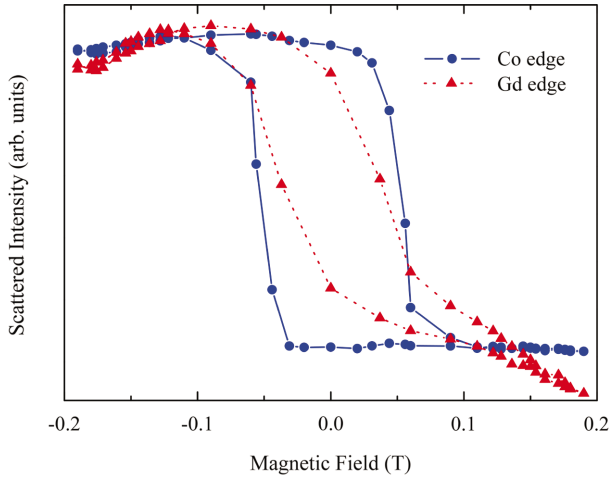

Figure 6
Magnetization curves recorded at the Co (circles) and the Gd (diamond) edges at 66 K.

adjusting the scattering angle it was possible to enhance the contribution of the probe layer. In this example the angle of incidence of the incoming photons was adjusted to 14° and 7° for the Co and the Gd magnetization curves, respectively. At room temperature the Gd film does not show any magnetic order. Well below the Curie temperature of Gd (∼250 K) we observed hysteresis loops from the Gd film and surprisingly an increase in the coercivity of the Co film. The full investigation will focus on the magnetic properties of the Cr layer by combining angular- and energy-dependent measurements at the Cr $L_{2,3}$ edge.

4. Conclusion

We have developed and tested a versatile in-vacuum reflectometer dedicated to X-ray resonant magnetic reflectivity. The project was primarily developed to extend the magneto-optic Kerr experiment technique into the soft X-ray range and, with the special design of the magnet, to carry out measurements in the longitudinal and transverse modes without changing the magnetic device or the position of the sample. These manipulations may change the conditions of the measurements and can be a problem in the case of a quantitative analysis of the combination of the LMOKE and TMOKE (longitudinal and transverse magneto-optic Kerr effects, respectively) data to develop a vectomagnetometry.

Owing to the large volume of the UHV chamber, further developments of the actual instrument are underway. It is planned to install another circle on the 2θ arm in order to extend the reciprocal space accessible with this instrument. In particular, we will access the domain of the reciprocal space usually forbidden by performing off-specular scattering (rocking-curve measurements) in a classsical $\theta/2\theta$ configuration. Another motivation is to perform a polarization analysis of the scattered X-rays by implementing a multilayer analyser on the 2θ arm (Korthright *et al.*, 1995). This will offer experimentalists a rather unique capability of separating the magnetic contribution from the dominating charge one in a diffraction pattern. Regarding the high flux that is already available at third-generation synchrotron radiation sources, the loss in scattered intensity owing to the efficiency of the analysers should be acceptable.

We would like to point out that this apparatus may also be used for non-magnetic anomalous scattering investigations in the soft X-ray range in order to profit from the huge contrast occurring at the absorption edges available in this energy range. The apparatus is currently installed in the Swiss Light Source and is planned to be transferred to the new French synchrotron source SOLEIL.

The authors would like to thanks L. Sève and F. Bartolomé for their contribution in the early conception stage of the apparatus, as well as F. Scheurrer for his advice about coils under vacuum, and O. Cugat for his collaboration concerning the magnetic device. One of us (NJ) is particularly in debt to X. Bicquart for his help with Linux problems. We wish to thank H. Fischer, G. Suciu and J. Voiron for providing us with the different test samples.

References

Bontempi, E., Jaouen, N. & Tonnerre, J. M. (2004). In preparation.
Déchelette, A., Saint-Lager, M. C., Tonnerre, J. M., Patrat, G., Raoux, D., Fischer, H., Andrieu, S. & Piecuch, M. (1999). *Phys. Rev. B*, **60**, 6623–6635.
Déchelette, A., Tonnerre, J. M., Saint-Lager, M. C., Bartolomé, F., Sève, L., Raoux, D., Fischer, H., Piecuch, M., Chakarian, V. & Kao, C. C. (1999). *Phys. Rev. B*, **60**, 6636–6645.
Dürr, H. A., Dudzik, E., Dhesy, S. S., Goedkoop, J. B., van der Laan, G., Belakhovsky, M., Mocuta, C., Marty, A. & Samson, Y. (1999). *Science*, **284**, 2166–2168.
Fischer, H. (1995). PhD thesis, Université Henri Poincaré-Nancy, France.
Goulon, J., Brookes, N. B., Gauthier, C., Goedkoop, J., Goulon-Ginet, C., Hagelstein, M. & Rogalev, A. (1995). *Physica B*, **208/209**, 199–202.
Grabis, J., Nefedov, A. & Zabel, H. (2003). *Rev. Sci. Instrum.* **74**, 4048–4051.
Hase, T. P., Pape, I., Read, D. E., Tanner, B. K., Dürr, H., Dudzik, E., van der Laan, G., Marrows, C. H. & Hickey, B. J. (2000). *Phys. Rev. B*, **61**, R3792–R3795.
Jaouen, N., Tonnerre, J. M., Raoux, D., Ortega, L., Bontempi, E., Müenzenberg, M., Felsch, W., Suzuki, M., Maruyama, H., Dürr., H. A., Dudzik, E. & van der Laan, G. (2001). *Appl. Phys. A*, **73**, 711–715.
Johnson, E. D., Kao, C. C. & Hastings, J. B. (1992). *Rev. Sci. Instrum.* **63**, 1443–1446.
Kao, C. C., Chen, C. T., Johnson, E. D., Hastings, J. B., Lin, H. J., Ho, G. H., Meigs, G., Brot, J. M., Hulbert, S. L., Ydzerda, Y. U. & Vettier, C. (1994). *Phys. Rev. B*, **50**, 9599–9602.
Kao, C. C., Hastings, J. B., Johnson, E. D., Siddons, D. P., Smith, G. C. & Prinz, G. A. (1990). *Phys. Rev. Lett.* **56**, 373–376.
Kortright, J. B. & Kim, S.-K. (2000). *Phys. Rev. B*, **62**, 12216–12228.
Korthright, J. B., Rice, M. & Franck, K. D. (1995). *Rev. Sci. Instrum.* **66**, 1567–1569.
Quitmann, C., Fleschsig, U., Patthey, L., Schmidt, T., Ingold, G., Howells, M., Janousch, M. & Abela, R. (2001). *Surf. Sci.* **480**, 173–179.
Roper, M. D., van der Laan, G., Durr, H. A., Dudzik, E., Collins, S. P., Miller, M. C. & Thomson, S. P. (2001). *Nucl. Instrum. Methods*, A**467/468**, 1101–1104.
Sacchi, M., Spezzani, C., Torelli, P., Avila, A., Delaunay, R. & Hague, C. F. (2003). *Rev. Sci. Instrum.* **74**, 2791–2795.
Sève, L., Tonnerre, J. M., Raoux, D., Bobo, J. F., Piecuch, M., De Santis, M., Troussel, P., Brot, J. M., Chakarian, V., Kao, C. C. & Chen, C. T. (1995). *J. Magn. Magn. Mater.* **148**, 68–69.
Sirotti, F., Polack, F., Cantin, J. L., Sacchi, M., Delaunay, R., Meyer, M. & Liberati, M. (2000). *J. Synchrotron Rad.* **7**, 5–11.
Spezzani, C., Torelli, P., Sacchi, M., Delaunay, R., Hague, C. F., Cros, V. & Petroff, F. (2002). *Appl. Phys. Lett.* **81**, 3425–3427.
Tonnerre, J. M., Jergel, M., Raoux, D., Idir, M., Soullié, G., Barchewitz, R. & Rodmacq, B. (1993). *J. Magn. Magn. Mater.* **68**, 230–233.
Tonnerre, J. M., Sève, L., Raoux, D., Soullié, G., Rodmacq, B. & Wolfers, P. (1995). *Phys. Rev. Lett.* **75**, 740–743.

Received 19 November 2003 • Accepted 7 June 2004